nature physics

SUPPLEMENTARY INFORMATION

https://doi.org/10.1038/s41567-019-0564-y

In the format provided by the authors and unedited.

Observation of nodal-line semimetal with ultracold fermions in an optical lattice

Bo Song[1,6], Chengdong He[1,6], Sen Niu[2,3,6], Long Zhang[2,3], Zejian Ren[1], Xiong-Jun Liu[2,3,4,5]* and Gyu-Boong Jo[1]*

[1]Department of Physics, The Hong Kong University of Science and Technology, Hong Kong, China. [2]International Center for Quantum Materials, School of Physics, Peking University, Beijing, China. [3]Collaborative Innovation Center of Quantum Matter, Beijing, China. [4]CAS Center for Excellence in Topological Quantum Computation, University of Chinese Academy of Sciences, Beijing, China. [5]Institute for Quantum Science and Engineering and Department of Physics, Southern University of Science and Technology, Shenzhen, China. [6]These authors contributed equally: Bo Song, Chengdong He, Sen Niu. *e-mail: xiongjunliu@pku.edu.cn; gbjo@ust.hk

Supplementary Information: Observation of nodal-line semimetal with ultracold fermions in an optical lattice

Bo Song,[1,*] Chengdong He,[1,*] Sen Niu,[2,*] Long Zhang,[2] Zejian Ren,[1] Xiong-Jun Liu,[2,3,4,5,†] and Gyu-Boong Jo[1,‡]

[1] *Department of Physics, The Hong Kong University of Science and Technology, Clear Water Bay, Kowloon, Hong Kong SAR*

[2] *International Center for Quantum Materials, School of Physics, Peking University, Beijing, China*

[3] *Collaborative Innovation Center of Quantum Matter, Beijing 100871, China*

[4] *CAS Center for Excellence in Topological Quantum Computation, University of Chinese Academy of Sciences, Beijing 100190, China*

[5] *Institute for Quantum Science and Engineering and Department of Physics, Southern University of Science and Technology, Shenzhen 518055, China*

(Dated: July 22, 2019)

Contents

*These authors contributed equally to this work.
†Electronic address: xiongjunliu@pku.edu.cn
‡Electronic address: gbjo@ust.hk

I. Methods for numerical simulations

A. Plane wave expansion calculation

We first consider the situation without trapping potential. The trap effect will be discussed later. The 2D optical lattice and Raman potential take the form

$$\begin{aligned} H_{\text{lattice}} &= \sum_{\sigma=\uparrow,\downarrow} V_{x\sigma}\cos^2(k_0 x) + V_{y\sigma}\cos^2(k_0 y) \\ V_R &= M_R \cos k_0 x \exp\left(ik_1 y + ik_2 z\right)|\downarrow><\uparrow| + \text{H.c.}, \end{aligned} \tag{S1}$$

where $k_1 = k_0\cos\theta$, $k_2 = k_0\sin\theta$, and $\theta = 68°$. The total Hamiltonian including the kinetic and Zeeman energy takes the form

$$H_{\text{total}} = H_{\text{lattice}} + V_R + \sum_{\sigma=\uparrow,\downarrow} \frac{p_{x\sigma}^2 + p_{y\sigma}^2 + p_{z\sigma}^2}{2m} + m_z(|\uparrow><\uparrow| - |\downarrow><\downarrow|). \tag{S2}$$

The Hamiltonian can be diagonalized in the plane-wave basis, labelled by the momentum and spin. In the numerical simulation, the zero point of the effective Zeeman energy m_z is shifted by the on-site energy difference between spin-up and spin-down, caused by the spin-dependent lattice potential, at $M_R = 0$. The optical lattice potential couples the plane waves of the same spin with momentum difference $(\pm 2k_0, 0, 0)$ or $(0, \pm 2k_0, 0)$, while the Raman potential does for the opposite spin with momentum difference $(\pm k_0, k_1, k_2)$. As a result, the Bloch states of the n-th band with the (quasi-)momentum (q_x, q_y, k_z) take the form

$$\begin{aligned} |\psi_{q_x,q_y,k_z,n}\rangle = \sum_{M,N} \big[&\phi_{q_x,q_y,k_z,n}(M,N,\uparrow)|q_x + 2Mk_0, q_y + 2Nk_0, k_z + k_2/2, \uparrow\rangle \\ &+ \phi_{q_x,q_y,k_z,n}(M,N,\downarrow)|q_x + k_0 + 2Mk_0, q_y - k_1 + 2Nk_0, k_z - k_2/2, \downarrow\rangle\big]. \end{aligned} \tag{S3}$$

Here M, N are integers, and $\phi_{q_x,q_y,k_z,n}(M,N,\sigma)$ denotes the coefficient of the corresponding plane-wave basis. The spin polarization is measured along z direction. The spin polarization for the Bloch state is calculated from

$$\begin{aligned} S_z(q_x,q_y,k_z,n) &= \langle\psi_{q_x,q_y,k_z,n}|\hat{\sigma}_z|\psi_{q_x,q_y,k_z,n}\rangle \\ &= \sum_{M,N} |\phi_{q_x,q_y,k_z,n}(M,N,\uparrow)|^2 - \sum_{M,N} |\phi_{q_x,q_y,k_z,n}(M,N,\downarrow)|^2. \end{aligned} \tag{S4}$$

The spin texture in equilibrium is calculated from the density matrix ρ with matrix elements $\rho(q_x, q_y, k_z, n; q_x', q_y', k_z', n')$ in Bloch eigenstates. For equilibrium states, ρ is diagonal and the matrix elements take the form $\rho(q_x, q_y, k_z, n; q_x, q_y, k_z, n)$. The numerical results shown in Fig. 3(a,d) in main text are calculated with temperature $T = 0.35E_r$ and chemical potential $\mu = 0.5E_r$. For the quench dynamics, we have considered two cases. First, we consider no decay of momentum distribution on k_z, so k_z is taken as a good quantum number and the density matrix elements take the form $\rho(q_x, q_y, k_z, n; q_x, q_y, k_z, n')$. The spin texture of a single k_z layer is calculated by

$$S_z(q_x, q_y, k_z) = \frac{\text{Tr}_n(\hat{\sigma}_z\rho)}{\text{Tr}_n\rho}, \tag{S5}$$

and the observable spin texture with k_z integrated out is calculated by

$$S_z(q_x, q_y) = \frac{\text{Tr}_{k_z}[\text{Tr}_n(\hat{\sigma}_z\rho)]}{\text{Tr}_{k_z}[\text{Tr}_n\rho]}. \tag{S6}$$

On the other hand, we consider that the momentum distribution of k_z has decay, and the density matrix elements take the form $\rho(q_x, q_y, k_z, n; q_x, q_y, k_z', n')$. In this case, the observed spin texture with k_z integrated out can still be calculated by Eq. (S6). In both cases, the lowest five bands are taken into account for both pre-quench and post-quench Hamiltonians.

B. Tight binding model

Besides the two-dimensional lattice, atoms are also distributed along the z direction. The spin-up plane wave with z-directional kinetic energy $\hbar^2(k_z+k_2/2)^2/2m$ is coupled with spin-down plane wave with $\hbar^2(k_z-k_2/2)^2/2m$. Therefore the kinetic energy difference in the z direction can be interpreted as an effective Zeeman term. The tight binding Hamiltonian in the lattice site (x,y) with momentum $k_z+\sigma k_2/2$ in the z direction has the form [1].

$$\begin{aligned}H_{\mathrm{TB}} =& -\sum_{x,y,k_z}\left(t_{x\uparrow}c^{\dagger}_{x,y,k_z,\uparrow}c_{x+1,y,k_z,\uparrow}+t_{x\downarrow}c^{\dagger}_{x,y,k_z,\downarrow}c_{x+1,y,k_z,\downarrow}+t_{y\uparrow}c^{\dagger}_{x,y,k_z,\uparrow}c_{x,y+1,k_z,\uparrow}+t_{y\downarrow}c^{\dagger}_{x,y,k_z,\downarrow}c_{x,y+1,k_z,\downarrow}\right)\\ &+\sum_{x,y,k_z}(-1)^x e^{ik_1 y}t_{so}(c^{\dagger}_{x,y,k_z,\uparrow}c_{x+1,y,k_z,\downarrow}-c^{\dagger}_{x,y,k_z,\uparrow}c_{x-1,y,k_z,\downarrow})+\mathrm{H.c.}\\ &+\sum_{x,y,k_z,\sigma}\left[\frac{\hbar^2(k_z+\sigma k_2/2)^2}{2m}+\sigma m_z\right]c^{\dagger}_{x,y,k_z,\sigma}c_{x,y,k_z,\sigma}.\end{aligned} \tag{S7}$$

Under the Fourier transformation $c_{x,y,k_z,\sigma}=N_L^{-1/2}\sum_{q_x,q_y,k_z}e^{iq_x x+iq_y y}c_{q_x,q_y,k_z,\sigma}$ where N_L denotes the number of lattice sites, the above Hamiltonian in the quasi-momentum space has the form

$$\begin{aligned}H_{\mathrm{TB}} =& -\sum_{q_x,q_y,k_z}\left[(2t_{x\uparrow}\cos q_x a+2t_{y\uparrow}\cos q_y a)c^{\dagger}_{q_x,q_y,k_z,\uparrow}c_{q_x,q_y,k_z,\uparrow}+(2t_{x\downarrow}\cos q_x a+2t_{y\downarrow}\cos q_y a)c^{\dagger}_{q_x,q_y,k_z,\downarrow}c_{q_x,q_y,k_z,\downarrow}\right]\\ &+\sum_{q_x,q_y,k_z}2it_{so}\sin(q_x a-\pi)c^{\dagger}_{q_x,q_y,k_z,\uparrow}c_{q_x-\pi,q_y-k_1,k_z,\downarrow}-2i\sin(q_x a-\pi)c^{\dagger}_{q_x-\pi,q_y-k_1,k_z,\downarrow}c_{q_x,q_y,k_z,\uparrow}\\ &+\sum_{q_x,q_y,k_z,\sigma}\left[\frac{\hbar^2(k_z+\sigma k_2/2)^2}{2m}+\sigma m_z\right]c^{\dagger}_{q_x,q_y,k_z,\sigma}c_{q_x,q_y,k_z,\sigma}\end{aligned} \tag{S8}$$

The Bloch Hamiltonian can be further obtained as

$$H_{\mathrm{TB}}=\sum_{q_x,q_y,k_z}\begin{pmatrix}c^{\dagger}_{q_x,q_y,k_z,\uparrow} & c^{\dagger}_{q_x-\pi,q_y-k_1,k_z,\downarrow}\end{pmatrix}H_{q_x,q_y,k_z}\begin{pmatrix}c_{q_x,q_y,k_z,\uparrow}\\ c_{q_x-\pi,q_y-k_1,k_z,\downarrow}\end{pmatrix}, \tag{S9}$$

where H_{q_x,q_y,k_z} can be expressed in terms of the Pauli matrices

$$\begin{aligned}H_{q_x,q_y,k_z} =& \left[m_z-2t_{x+}\cos q_x a+2t_{y+}\cos(q_y a-\phi_+)+\sin\theta k_z\right]\sigma_z\\ &+2t_{so}\sin q_x a\sigma_y\\ &+\left[-2t_{x-}\cos q_x a+2t_{y-}\cos(q_y a+\phi_-)+k_z^2+\sin^2\theta/4\right]\sigma_0.\end{aligned} \tag{S10}$$

Here to facilitate the further discussion we have taken that $k_0=1$, the recoil energy $E_r=1$, the hopping coefficients $2t_{x\pm}=t_{x\uparrow}\pm t_{x\downarrow}$, $2t_{y\pm}=\sqrt{(t_{y\downarrow}\sin k_1 a)^2+(t_{y\uparrow}\pm t_{y\downarrow}\cos k_1 a)^2}$, and $\tan\phi_{\pm}=\frac{t_{y\downarrow}\sin k_1 a}{t_{y\uparrow}\pm t_{y\downarrow}\cos k_1 a}$. If the Bloch momentum q_y is shifted as $q_y\to q_y+\phi_+/a$, one obtains the Bloch Hamiltonian Eq. (1) shown in the main text

$$\begin{aligned}H_{q_x,q_y,k_z} =& \left[m_z-2t_{x+}\cos q_x a+2t_{y+}\cos q_y a+\sin\theta k_z\right]\sigma_z\\ &+2t_{so}\sin q_x a\sigma_y\\ &+\left[-2t_{x-}\cos q_x a+2t_{y-}\cos(q_y a+\phi_-+\phi_+)+k_z^2+\sin^2\theta/4\right]\sigma_0,\end{aligned} \tag{S11}$$

of which the positions of Dirac points (nodal lines) are symmetric in q_y direction. In the experiment, the p bands which are not included in the two band tight binding model, are coupled with s bands by Raman potential and will slightly move the positions of Dirac points (nodal lines) compared to the tight binding model.

C. Lindblad master equations

For the non-equilibrium case, in order to phenomenologically simulate the decay effect from upper to lower bands during the quench dynamics, we introduce the Lindblad master equation which describes the evolution of single

particle density matrix. The equation that describes an inter-band oscillation and decay from higher to lower bands takes the form

$$\dot{\rho} = -i[H,\rho] + \sum_n \gamma[L_n \rho L_n^\dagger - \frac{1}{2}\{L_n^\dagger L_n, \rho\}]. \tag{S12}$$

Here ρ is a time dependent density matrix, $L_n = |n\rangle\langle n+1|$, and n denotes the band index. In this case we neglect the momentum scattering caused by trapping potential and coupling with photons and other environments, thus lattice momentum (q_x, q_y, k_z) are good quantum numbers and momentum indices are omitted in the formula. The initial density matrix is determined by the pre-quench Fermi distribution. The pre-quench single particle density matrix is determined by temperature T and chemical potential μ, values of which are similar to experiment settings. In this case, time-dependent spin polarization for a k_z layer after quench is calculated by Eq. (S5) using the density matrix calculated from Eq. (S12). In order to simulate the time-averaged spin texture in experiment shown in Fig. 4(a), we should calculate the k_z integrated time-averaged spin texture. In principle it is difficult to calculate the exact distribution of k_z during time evolution, which depends on many factors such as the effects of trapping potential and the coupling with photons and other environments. Nevertheless, in the last several periods of spin relaxation close to steady state, the dominant k_z distribution must be around k_z dispersion minimum and the dominant dynamics is just the inter-band oscillation as can be seen from Fig. 4(e) and grey curves in Fig. 4(f). Therefore We approximate the time-averaged spin texture with

$$\bar{S}_z(q_x, q_y) = \int_{t_i}^{t_f} dt \int_{-\delta}^{\delta} dk_z \frac{\mathrm{Tr}_n \hat{\sigma}_z \rho}{\mathrm{Tr}_n \rho}, \tag{S13}$$

where $[-\delta, \delta]$ is a small k_z integration interval around post-quench k_z dispersion minimum for the white curves (zero polarization curves) as shown in Fig. S3 (b,c,d), $t \in [t_i, t_f]$ is the time integration interval for several final periods. We show in the main text the numerical result of the time-averaged spin texture $\bar{S}_z(q_x, q_y)$ in Fig. 4(b), with parameters $m_z = 0.27E_r$, $\delta = 0.32k_0$. We also determine the (q_x, q_y) positions of the white curve from the time averaged spin texture of the $k_z = 0$ layer, as shown in right-down corner of Fig. 4(f).

In order to further interpret the evolution of the oscillation center of experimental result shown in Fig. 4(e), we include the decay effect along k_z. From the pre- and post-quench equilibrium Fermi distribution in Fig. S3, one can see that the band minimum depends on k_z. When $|m_z|$ is not quite large, the center of the particle number distribution is around $k_z = 0$ on the white curves of the static spin texture. While in the deep trivial case where $m_z \approx -4.6E_r$, there exist no white curves and the k_z distribution center is away from $k_z = 0$, as is shown in Fig. S3(a). Finally, we phenomenologically add a decay term to the previous Lindblad form master equation Eq. (S12),

$$\begin{aligned}\dot{\rho} = &- i[H,\rho] + \sum_n \gamma[L_n \rho L_n^\dagger - \frac{1}{2}\{L_n^\dagger L_n, \rho\}] \\ &+ \sum_{k_{z_i}=k_{z_2}}^{k_{z_n}} \gamma_z[L_{k_{z_i}} \rho L_{k_{z_i}}^\dagger - \frac{1}{2}\{L_{k_{z_i}}^\dagger L_{k_{z_i}}, \rho\}].\end{aligned} \tag{S14}$$

Here discrete $k_{z_i} \in [k_{z_1}, k_{z_n}]$ is taken, $L_{k_{zi}} = \sum_n |q_x, q_y, k_{z_i}, n\rangle\langle q_x, q_y, k_{z_{i-1}}, n|$, $L_n = \sum_{k_{z_i}} |q_x, q_y, k_{z_i}, n\rangle\langle q_x, q_y, k_{z_i}, n+1|$, and q_x, q_y are still good quantum numbers. The initial density matrix is determined by the pre-quench Fermi distribution. Such Lindblad operator can be used to phenomenologically simulate the decay of k_z from dispersion minimum of the pre-quench Hamiltonian to that of the post-quench Hamiltonian. In this case, the time evolution for the observed spin polarization is calculated from Eq. (S6) using the density matrix calculated by Eq. (S14). We show in the main text the numerical result of the time evolution for spin polarization by green curve in Fig. 4(f) with parameters $m_z = 0.27E_r$, $\gamma = 0.01$, $\gamma_z = 0.05$, where the (q_x, q_y) positions of the white curve are taken from the time averaged spin texture of the $k_z = 0$ layer, as shown in right-down corner of Fig. 4(f).

II. 2D Dirac semimetal phase and 3D nodal line semimetal phase

A. Equilibrium state

In this section, we provide the theoretical description for both 2D Dirac semimetal and 3D nodal line semimetal phases, and show how to reconstruct 3D nodal line semimetal phases from a set of 2D Dirac semimetal phase measurements. We first prove that the spin texture with k_z integrated measured in experiment is equivalent to the spin texture with single $k_z = 0$ layer, and further the measured k_z integrated spin textures with different Zeeman energies m_z are equivalent to the 2D spin textures with different k_z but fixed m_z. The results are valid in the presence of trapping. Therefore we can effectively reconstruct the 3D topological structure from a series of measurements of integrated spin texture, which results in the k_z-layer resolved spin-textures.

1. The two-dimensional Dirac semimetal phase

The Dirac points in a 2D layer with specific k_z can be characterized by the topological phase transition points of a 1D Hamiltonian H_{q_y}, which is reduced from the original 2D Hamiltonian in a certain k_z layer as,

$$H = [m_z - 2t_{x+}\cos q_x a + 2t_{y+}\cos(q_y a - \phi_+) + \sin\theta k_z]\,\sigma_z + 2t_{so}\sin q_x a\sigma_y, \tag{S15}$$

where σ_0 term has been discarded since it does not contribute to gap closing and has no effect on topology. Now the dimension reduction operation of the 2D Hamiltonian is performed by taking q_y as a parameter, thus the 1D Hamiltonian for a specific q_{y_0} reads

$$H_{q_{y_0}} = \overrightarrow{\mathbf{h}}\cdot\overrightarrow{\boldsymbol{\sigma}} = h_z\sigma_z + h_y\sigma_y = [m_z'(q_{y_0}) - 2t_{x+}\cos q_x a]\sigma_z + 2t_{so}\sin q_x a\sigma_y. \tag{S16}$$

The above 1D static topological phase is classified by integer invariants in the Altland-Zirnbauer (AZ) symmetry classes [3]. The 1D winding number that characterizes the topology is defined as

$$\upsilon_{q_{y_0}} = \frac{1}{4\pi}\int_{\mathrm{BZ}} dq_x \mathrm{Tr}[\sigma_x\mathbb{H}_{q_{y_0}}\mathrm{d}\mathbb{H}_{q_{y_0}}], \tag{S17}$$

where $\mathbb{H}_{q_{y_0}} = \overrightarrow{\mathbf{h}}/|\overrightarrow{\mathbf{h}}|\cdot\overrightarrow{\boldsymbol{\sigma}}$ is normalized Hamiltonian. The winding number is formulated by a mapping from the BZ, which is a 1D torus T^1, to the 1D spherical surface S^1 through the unit vector field

$$\overrightarrow{\mathbf{n}}(k) = \overrightarrow{\mathbf{h}}/|\overrightarrow{\mathbf{h}}|. \tag{S18}$$

The topological number counts the times that the mapping covers the spherical surface S^1. To determine the topology of the 1D Hamiltonian, here we use the concept "band inversion surface (BIS)" introduced in [2]. Here the BIS is defined by q_x points in the 1D FBZ by solving $h_z(q_x, q_{y_0}) = 0$. In our 1D model, the BISs are discrete intersections between the white curves and the straight line $q_y = q_{y_0}$, and the non-trivial winding number requires the existence of two symmetric BISs along q_x direction. After defining the h' term

$$h'(q_x, q_y) = -2t_{x+}\cos q_x a + 2t_{y+}\cos(q_y a - \phi_+) \tag{S19}$$

contained in the h_z term, it is easy to verify that when $-\max[h'(q_x, q_{y_0})] < m_z + \sin\theta k_z < -\min[h'(q_x, q_{y_0})]$, $\quad q_x \in [-k_0, k_0]$, the winding number is non-zero as shown in the right hand side of Fig. S1(a,b). In experiment, the existence of BISs can be monitored by looking at spin-balanced points in the equilibrium spin texture.

In a single 2D k_z layer, the BIS points form curves. The BIS curves in a 2D layer can be taken as a "bulk correspondence" of the Fermi arc in time-reversal breaking 2D semimetals. The 3D time-reversal breaking Weyl semimetals can usually be viewed as stacked 2D Chern insulators in a third direction. The Fermi arc is formed by non-trivial chiral edge states varying as a function of the momentum in the third direction, and the Weyl nodes are

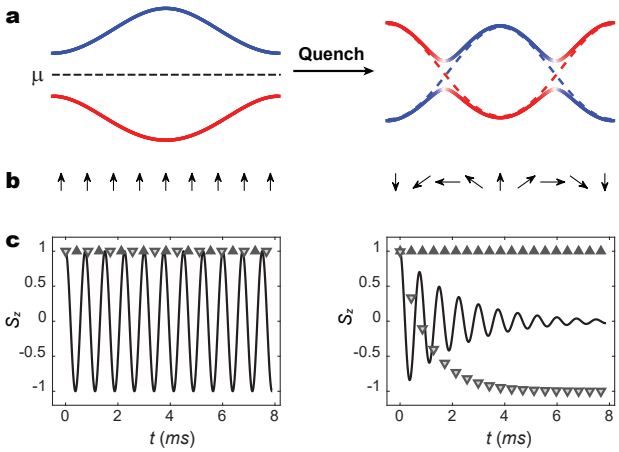

Figure S1: Sketch for characterization of the 1D topological phase. (a) Trivial (left) and non-trivial (right) 1D bands in q_x direction with fixed q_y and k_z as parameters. In the quench experiment, the Hamiltonian of the dominant $k_z = 0$ layer is prepared in a deep trivial regime and quenched to a non-trivial regime, during which for a part of 1D Hamiltonians the band inversion occurs and topological gap is opened. (b) Trivial (left) and non-trivial (right) 1D windings determined by the vector field in Eq. (S18). (c) Quench dynamics simulated by the 2D tight binding model in Eq. (S10) with $(t_{x\uparrow}, t_{x\downarrow}, t_{y\uparrow}, t_{y\downarrow}, t_{so}) = (0.14, 0.16, 0.13, 0.11, 0.1)E_r$ and with fixed $k_z = 0$. m_z is quenched from $-9.2E_r$ to $0.27E_r$. $\gamma = 0$ for the left subfigure and $\gamma = 0.04$ for the right subfigure. The green solid curve corresponds to the point $(q_x, q_y, k_z) = (-0.35, 0.187, 0)k_0$ and its time average spin polarization is zero. The up-pointing and down-pointing triangles correspond to the point $(q_x, q_y, k_z) = (0, 0.187, 0)k_0$ and $(q_x, q_y, k_z) = (-1, 0.187, 0)k_0$ respectively. In the $\gamma > 0$ case the density matrix will decay towards the lowest band.

exactly at the transition point of the 2D Chern insulators. Similar to the case for the Weyl semimetals, the existence of Dirac points in the 2D layer also reflects the topological phase transitions of the reduced 1D H_{q_y} Hamiltonians. As functions of parameter q_y, the BIS points of the 1D reduced Hamiltonians form white curves in 2D (q_x, q_y) plane. If the two BISs touch and then disappear, the 1D winding number changes and the gap should close at the transition point. The gapless points are exactly the Dirac points in our model. Due to the reflection symmetry along $q_x = 0$ axis, the Dirac points can only appear at $q_x = 0$ or $\pm k_0$. With specific m_z, the Dirac points exist when $-\max[h'(sk_0, q_y)] < m_z + \sin\theta k_z < -\min[h'(sk_0, q_y)]$, $\quad q_y \in [-k_0, k_0]$, where $s = 0$ or ± 1 corresponds to Dirac points located at $q_x = 0$ or $\pm k_0$.

To define the topological invariant of the Dirac points (q_{x1}, q_{y1}) in a k_z layer, we choose a closed clockwise loop $\mathcal{C}$ in the q_x-q_y plane that only wraps the Dirac point (q_{x1}, q_{y1}). Expanding the Hamiltonian around the degenerate point, one obtains the continuously deformed Hamiltonian

$$H = \mathbf{q} \cdot \boldsymbol{\sigma} = s_1 \epsilon_z \sigma_y + s_2 \epsilon_x \sigma_y, \tag{S20}$$

where $(\epsilon_y, \epsilon_x) = \epsilon(\cos\beta, i\sin\beta)$ form the loop $\mathcal{C}$ with radius ϵ, β is determined by (ϵ_y, ϵ_x), and both s_1, s_2 can be $+$ or $-$. The Dirac point can be characterized by the winding number

$$\upsilon_{\text{point}} = \frac{i}{2\pi\epsilon^2} \int_{\mathcal{C}} \mathbf{q}^* d\mathbf{q} = \pm \int_0^{2\pi} (\cos^2\beta + \sin^2\beta) d\beta = \pm 1, \tag{S21}$$

where the winding numbers ± 1 correspond to $s_1 s_2 = \pm 1$ respectively.

2. *The three-dimensional nodal line semimetal phase*

In our system, positions of Dirac points in the q_x-q_y plane depend on k_z, resulting nodal line structures. At $\sin q_x a = 0$ with $q_x = 0(\pm k_0)$, for any $q_y \in [-k_0, k_0]$, there exist a k_z where the tight binding Hamiltonian has

degenerate points. When q_y varies from $-k_0$ to k_0 the degenerate points form curves, which are called the nodal linew. We plot the positions of the nodal points in the 3D momentum space together with their projections onto the 2D planes with $m_z = 0$ in Fig. S2.

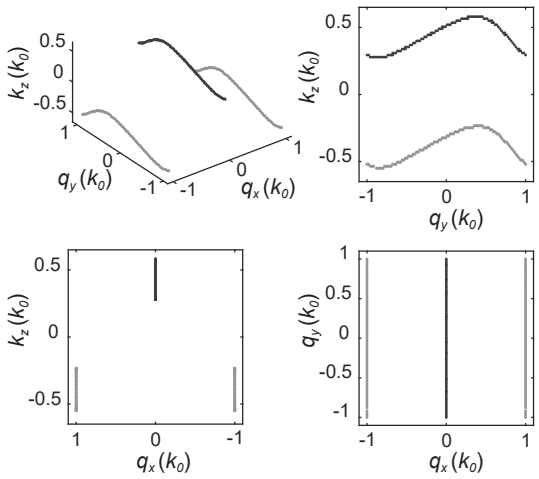

Figure S2: Positions of the nodal with $(V_{x\uparrow}, V_{x\downarrow}, V_{y\uparrow}, V_{y\downarrow}, M_R, m_z) = (2.3, 1.6, 2.3, 3.0, 0.68, 0)E_r$ in 3D momentum space, and their projections on three 2D planes. The results are calculated with plane wave expansion. The light grey and dark black curves correspond to $q_x = \pm k_0$ and 0 respectively.

To define the topological invariant of the nodal lines, similar to the former case for Dirac points, we select a degenerate point (q_{x1}, q_{y1}, k_{z1}) in the nodal lines with $q_{x1} = 0(\pm k_0)$, and choose a closed clockwise loop $\mathcal{C}$ in the q_x-k_z plane that wraps around the (q_{x1}, q_{y1}, k_{z1}) point but does not intersect with the nodal lines. After discarding the σ_0 terms and expanding the Hamiltonian near the (q_{x1}, q_{y1}, k_{z1}) point, one obtains the continuously deformed Hamiltonian

$$H = \mathbf{q} \cdot \boldsymbol{\sigma} = \epsilon_z \sigma_z \pm \epsilon_x \sigma_y, \tag{S22}$$

where $(\epsilon_z, \epsilon_x) = \epsilon(\cos\beta, i\sin\beta)$ form the loop $\mathcal{C}$ with radius ϵ, β is determined by (ϵ_z, ϵ_x), and $+(-)$ correspond to nodal lines with $q_{x1} = 0(\pm k_0)$. The nodal line can be characterized by the winding number

$$\upsilon_{\text{line}} = \frac{i}{2\pi\epsilon^2} \int_{\mathcal{C}} \mathbf{q}^* d\mathbf{q} = \pm \int_0^{2\pi} (\cos^2\beta + \sin^2\beta) d\beta = \pm 1. \tag{S23}$$

The winding numbers $+1(-1)$ correspond to nodal lines with $q_{x1} = 0(\pm k_0)$ respectively. The υ_{line} defined here can be related to the υ_{point} at the same degenerate point defined in former subsection via

$$\upsilon_{\text{line}} = \pm \upsilon_{\text{point}} \tag{S24}$$

if the $\mathcal{C}$ loops defined in each cases can be continuously deformed to each other. The $+$ sign is taken when the direction of the loop does not change after deformation, and the $-$ sign is taken when the direction of the loop changes.

3. Equivalence between $k_z = 0$ layer spin textures and k_z-integrated spin textures

Here we show that the static $k_z = 0$ layer spin textures and static k_z integrated spin textures are equivalent in the sense that their positions of white curves are exactly the same in the two-band model, yielding that positions of Dirac points are the same. Note that for a random single (q_x, q_y) point the k_z distribution centre may be away from $k_z = 0$ as shown in Fig. S3(a). It turns out that such (q_x, q_y) points are highly polarized and far away from white curves in the spin texture. Now we theoretically show that the positions of white curves are exactly the same for the $k_z = 0$

layer and the k_z integrated spin textures. From the tight binding model, the Hamiltonian at those spin-balanced momenta $(q_{x0}, q_{y_0}, 0)$ in the $k_z = 0$ layer reads

$$H_{q_{x0},q_{y0},0} = 0\sigma_z + 2t_{so} \sin q_x a \sigma_y, \tag{S25}$$

where the irrelevant terms have been discarded. With fixed 2D lattice momentum (q_{x_0}, q_{y_0}), the Hamiltonian at (q_{x0}, q_{y0}, k_z) points should be

$$H_{q_{x0},q_{y0},k_z} = \sin\theta k_z \sigma_z + k_z^2 \sigma_0 + 2t_{so} \sin q_x a \sigma_y. \tag{S26}$$

It is clear that the Hamiltonian satisfies an emergent magnetic group symmetry defined by

$$\mathcal{M}_z H_{q_{x0},q_{y0},k_z} \mathcal{M}_z^{-1} = H_{q_{x0},q_{y0},-k_z}, \tag{S27}$$

where $\mathcal{M}_z = \sigma_x K$. As a result the Bloch states at $\pm k_z$-momenta are degenerate but have opposite z-component spin polarizations. So after k_z is integrated the polarization will be kept zero at (q_{x0}, q_{y0}) point. Thus, the zero polarization (q_x, q_y) points for the $k_z = 0$ layer should also be zero polarized when k_z is integrated, resulting that the positions of white curves are the same in these two situations.

Note that in real optical lattice, the lowest two bands' spin polarizations may be affected due to the spin-orbit coupling between s and higher p bands. At the zero polarization positions $(k_{x0}, k_{y0}, 0)$ with finite temperature, the symmetric property of the energy and anti-symmetric property of the spin polarization with respect to k_z are slightly affected but the effect is tiny in the experimental parameter regime, as shown in Fig. S3. The positions of the white curves in the $k_z = 0$ layer and the k_z integrated case coincide in our plane-wave calculations [Fig. S4].

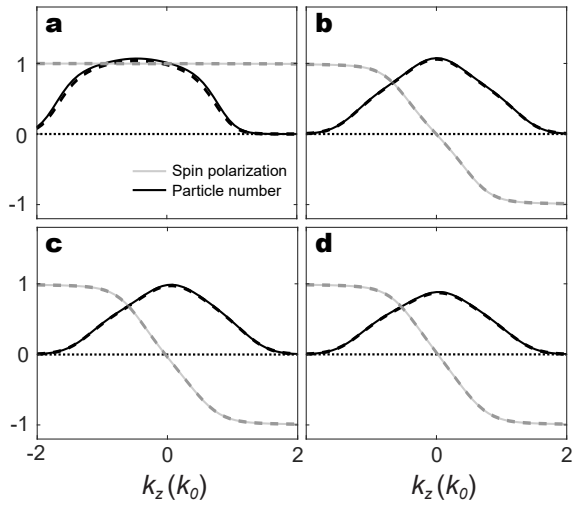

Figure S3: Particle number and spin polarization versus k_z at different (q_x, q_y) points without (solid lines) and with (dashed lines) z direction trap simulated with plane wave calculation. Parameters are set to $(V_{x\uparrow}, V_{x\downarrow}, V_{y\uparrow}, V_{y\downarrow}, M_R, m\omega_z^2 a^2/2, T) = (2.3, 1.6, 2.3, 3.0, 0.68, 0.002, 0.42)E_r$. (a) $m_z = -4.6E_r$, $(q_x, q_y) = (0.35, 0)k_0$. Due to large m_z, the $k_z = 0$ layer band is the deep trivial and there is no white curves structure in the spin texture. (b) $m_z = 0$, $(q_x, q_y) = (-0.475, -0.275)k_0$. (c) $m_z = 0.13E_r$, $(q_x, q_y) = (0.225, -0.475)k_0$. (d) $m_z = 0.27E_r$, $(q_x, q_y) = (0.275, 0.275)k_0$. In the figure (b)-(d) spin polarizations with k_z integrated are almost zero, thus the spin texture of $k_z = 0$ layer and of k_z integrated case have the same white curves structure. The chemical potentials in (a)-(d) are set to $\mu = [-0.34, 0.14, 0.14, 0.14]E_r$ when z direction trap is not included. When z direction trap is included, we keep particle number distribution unchanged to determine the chemical potentials.

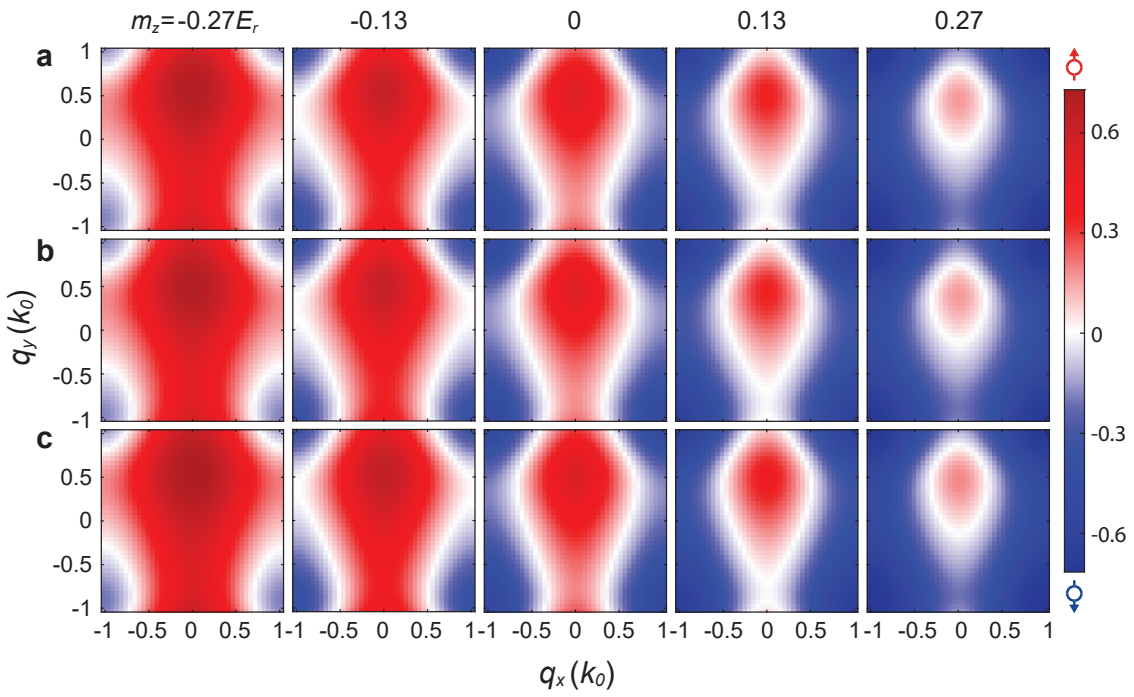

Figure S4: Comparison between the numerically simulated equilibrium spin textures calculated with plane waves. Parameters are set to $(V_{x\uparrow}, V_{x\downarrow}, V_{y\uparrow}, V_{y\downarrow}, M_R, m\omega_z^2 a^2, T) = (2.3, 1.6, 2.3, 3.0, 0.68, 0.004, 0.42)E_r$. (a) spin textures within the $k_z = 0$ layer without a trap along the z direction (upper row). (b) k_z integrated spin textures without a trap (middle row). (c) k_z integrated spin textures with a trap (lower row). Both the shapes and the locations of the white curves are almost the same in (a)-(c). For (a)-(b) without trap, $\mu = 0.14E_r$. For (c) with a z-directional trap included, we keep particle number distribution unchanged to determine the chemical potentials.

4. Equivalence between scanning of k_z and scanning of m_z

Here we show that m_z scan is equivalent to k_z scan due to the features of our model. The tight binding Hamiltonian H_{q_x,q_y,k_z,m_z} with parameters (q_x, q_y, k_z, m_z) has the form

$$\begin{aligned} H_{q_x,q_y,k_z,m_z} =& \left[-2t_{x+}\cos q_x a + 2t_{y+}\cos\left(q_y a - \phi_+\right) + \sin\theta k_z + m_z\right]\sigma_z \\ &+ 2t_{so}\sin q_x a\sigma_y \\ &+ \left[-2t_{x-}\cos q_x a + 2t_{y-}\cos\left(q_y a + \phi_-\right) + k_z^2 + \sin^2\theta/4\right]\sigma_0. \end{aligned} \tag{S28}$$

One can immediately obtain

$$H_{q_x,q_y,k_z,0} = H_{q_x,q_y,0,m_z} + \frac{m_z^2}{\sin^2\theta}\sigma_0, \tag{S29}$$

with the condition $m_z = \sin\theta k_z$, where both $k_0 = 1$ and $E_r = 1$ are assumed. The last constant σ_0 term can be discarded as an effective chemical potential. Finally one obtains

$$H_{q_x,q_y,k_z,0} = H_{q_x,q_y,0,m_z}, \tag{S30}$$

where $m_z = \sin\theta k_z$. The above equivalence is not restricted to tight binding model and also holds in the generic Bloch Hamiltonian, as can be easily seen from Eq. (S2). We plot the spin textures of $H_{q_x,q_y,k_z,0}$ and $H_{q_x,q_y,0,m_z}$ with the condition $m_z = \sin\theta k_z$ for both zero temperature and finite temperature cases to support the above statement in Fig. S5. From the results in Fig. S4 and Fig. S5 we find that the external trapping does not affect our conclusion, with more details given in the following subsection.

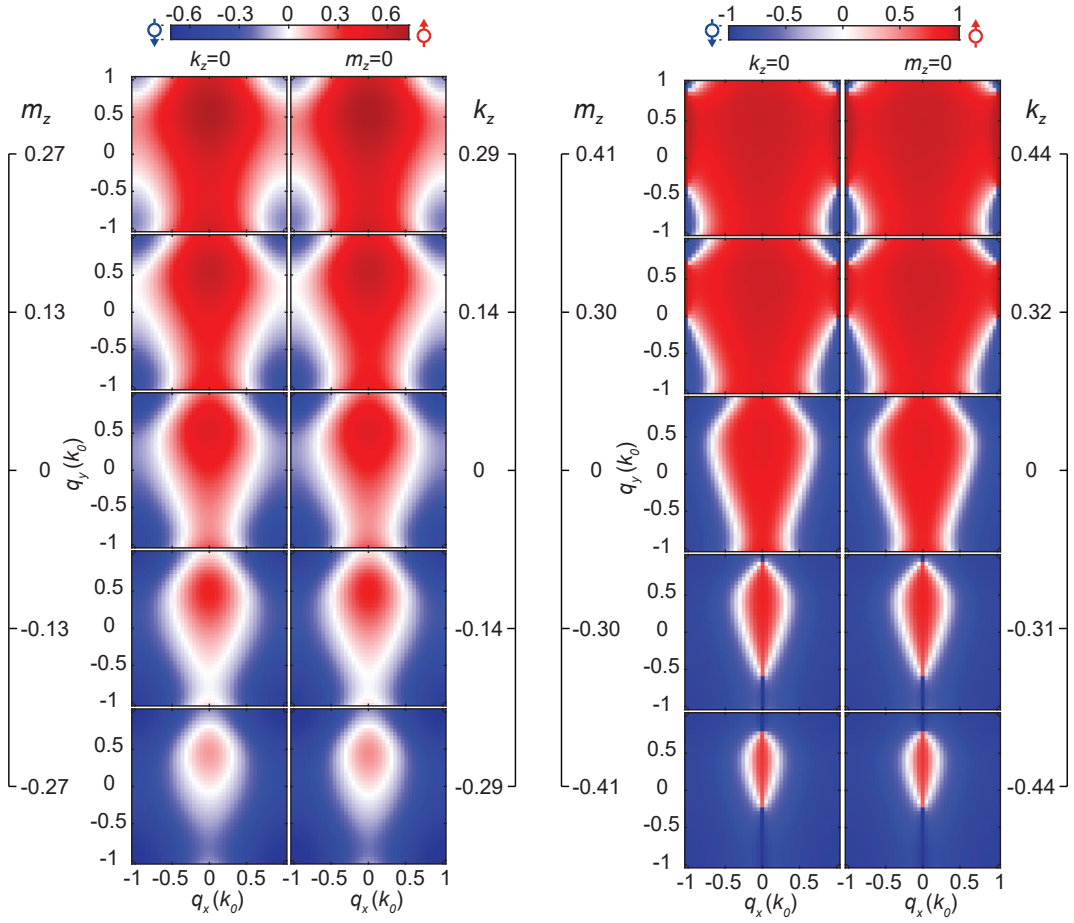

Figure S5: Comparison of simulated spin textures between $H_{q_x,q_y,k_z,0}$ and $H_{q_x,q_y,0,m_z}$, where m_z and k_z are in units of E_r and k_0 respectively, and are related by $m_z = \sin\theta k_z$. Optical lattice Raman potential parameters are set as $(V_{x\uparrow}, V_{x\downarrow}, V_{y\uparrow}, V_{y\downarrow}, M_R) = (2.3, 1.6, 2.3, 3.0, 0.68)E_r$. The left two columns correspond to finite temperature case with $T = 0.42E_r$, $\mu = 0.14E_r$, while the right two columns correspond the spin texture of the lowest band without temperature effect. For the finite temperature case, the m_z (effective m_z) from top to bottom is $(0.27, 0.13, 0, -0.13, -0.27)E_r$; for the latter case, the (effective) m_z from top to bottom is $(0.40, 0.27, 0, -0.27, -0.40)E_r$. The results are calculated with plane-wave expansion.

5. *Effect of trapping potential*

In the experiment, the trapping potential breaks the translation symmetry and the momentum k_z is no longer a good quantum number. Here we show that all our results obtained in the above sections are valid, not affected by the presence of the trapping, while the only modification is that we now refer k_z as to the projected momentum along z direction since it is not conserved. Before providing detailed proof, we qualitatively explain why our approach is not affected by the trapping. The essential reason is because the emergent magnetic group symmetry $\sigma_x K$ is not affected by the trapping potential $V_{\text{trap}}(\mathbf{r})$ which spin-independent for the present experiment and is real. Accordingly, the total Hamiltonian $\tilde{H}$, including the trapping potential, still preserves the emergent magnetic group symmetry. Note that the (quasi)momentum is no longer good quantum number due to trapping potential, but the spin texture can be defined by projecting the eigenstates onto the (quasi)momentum space which is actually resolved in the TOF imaging. The spin polarizations contributed from the projected $\pm k_z$ layers again cancel out due to the symmetry and the conclusion is not affected. This implies that the mixing between different k_z due to trapping cannot affect the integral result of the spin texture over all the k_z-momentum. Further, the shift of the projected k_z by m_z in the Bloch

Hamiltonian is clearly not affected by the trapping. Thus scanning m_z can still exactly map out the spin texture for each projected k_z layer (equivalent to the k_z layer without trapping). In this way, with our approach we can still reconstruct the 3D spin texture.

Now we provide the quantitative proof. In the present experiment, the trapping potential in z direction is a spin-independent harmonic trap V_{trap} of the form

$$V_{\text{trap}} = \frac{1}{2} m\omega_z^2 z^2, \tag{S31}$$

where the trapping strength is set to $m\omega_z^2 a^2 = 0.004E_r$ according to the experiment. For the tight binding model with the consideration of the trap, the Hamiltonian reads

$$H_{\text{TB}} = \sum_{q_x,q_y,k_z,k_z'} \begin{pmatrix} c^\dagger_{q_x,q_y,k_z,\uparrow} & c^\dagger_{q_x-\pi,q_y-k_1,k_z,\downarrow} \end{pmatrix} H_{q_x,q_y,k_z,k_z'} \begin{pmatrix} c_{q_x,q_y,k_z',\uparrow} \\ c_{q_x-\pi,q_y-k_1,k_z',\downarrow} \end{pmatrix}, \tag{S32}$$

where the matrix $H_{q_x,q_y,k_z,k_z'}$ has the form

$$\begin{aligned} H_{q_x,q_y,k_z,k_z'} =& \delta_{k_z,k_z'} \left[m_z - 2t_{x+} \cos q_x a + 2t_{y+} \cos q_y a + \sin\theta k_z \right] \sigma_z \\ &+ 2\delta_{k_z,k_z'} t_{so} \sin q_x a \sigma_y \\ &+ \delta_{k_z,k_z'} \left[-2t_{x-} \cos q_x a + 2t_{y-} \cos\left(q_y a + \phi_- + \phi_+\right) + k_z^2 + \sin^2\theta/4 \right] \sigma_0 \\ &+ V_{k_z,k_z'} \sigma_0, \end{aligned} \tag{S33}$$

and the real matrix elements of the trapping potential are calculated by

$$V_{k_z,k_z'} = \langle \psi_{k_z} | V_{trap} | \psi_{k_z'} \rangle. \tag{S34}$$

Here $|\psi_{k_z}\rangle$ denotes the z direction plane-wave basis with momentum k_z, which can be called projected k_z since it is not conserved in the presence of trapping. For a general spin-independent trapping potential as a real function of position z, one can prove that it satisfies the magnetic group symmetry $\sigma_x K$ either in momentum space or in position space. In momentum space, its matrix elements have the property

$$\begin{aligned} V_{k_{z1},k_{z2}} &= \int_{-\infty}^{+\infty} dz e^{-ik_{z1}z} e^{ik_{z2}z} V(z) \\ &= \left(\int_{-\infty}^{+\infty} dz e^{ik_{z1}z} e^{-ik_{z2}z} V(z) \right)^* \\ &= V^*_{-k_{z1},-k_{z2}}. \end{aligned} \tag{S35}$$

So the matrix $V_{k_z,k_z'}$ is invariant under the transformation $\sigma_x K$ after we replace all k_z by $-k_z$. Alternatively, to show that the trapping potential is invariant under the transformation $\sigma_x K$ in position space, one notes that the matrix elements of the trapping potential in position space are real. For the (q_x, q_y) points on the band inversion lines (white curves) with certain m_z, after neglecting the coefficients irrelevant with k_z for the σ_0 term, the Bloch Hamiltonian has the form

$$\begin{aligned} H_{q_x,q_y,k_z,k_z'} =& \delta_{k_z,k_z'} \sin\theta k_z \sigma_z + 2\delta_{k_z,k_z'} t_{so} \sin q_x a \sigma_y \\ &+ \left[\delta_{k_z,k_z'} (k_z^2 + \sin^2\theta/4) + V_{k_z,k_z'} \right] \sigma_0, \end{aligned} \tag{S36}$$

which is invariant after replacing k_z by $-k_z$ and under the transformation $\mathcal{M}_z = \sigma_x K$. Therefore, for an eigenstate $\psi\rangle = |\psi_\uparrow(k_z), \psi_\downarrow(k_z)\rangle$ of the Hamiltonian, the state $|\tilde{\psi}\rangle = \mathcal{M}_z|\psi_\uparrow(-k_z), \psi_\downarrow(-k_z)\rangle$ is also an eigenstate with the same eigenenergy. The magnetic group symmetry has the property $\mathcal{M}_z^2 = +1$ different from time reversal symmetry and the eigenstates are not necessarily doubly degenerate, i.e., $\mathcal{M}_z|\psi_\uparrow(-k_z), \psi_\downarrow(-k_z)\rangle$ may be either another eigenstate orthogonal to $|\psi_\uparrow(k_z), \psi_\downarrow(k_z)\rangle$, or equal to $|\psi_\uparrow(k_z), \psi_\downarrow(k_z)\rangle$ up to a global phase, depending on the the magnitude of

$t_{so}\sin q_x a$ and the eigenenergy (for details see Ref. [4]). We can calculate the expectation value of the spin polarization on the (q_x, q_y) point regardless of the detailed degeneracy with

$$\begin{aligned} S_z(q_x,q_y) =& \frac{\mathrm{Tr}_n(\hat{\sigma}_z\rho)}{\mathrm{Tr}_n(\rho)} = \frac{\mathrm{Tr}_n(\hat{\sigma}_z\mathcal{M}_z\rho\mathcal{M}_z^{-1})}{\mathrm{Tr}_n(\rho)} \\ =& \frac{\mathrm{Tr}_n(\mathcal{M}_z^{-1}\hat{\sigma}_z\mathcal{M}_z\rho)}{\mathrm{Tr}_n(\rho)} = -\frac{\mathrm{Tr}_n(\hat{\sigma}_z\rho)}{\mathrm{Tr}_n(\rho)} \\ =& -S_z(q_x,q_y) = 0, \end{aligned} \tag{S37}$$

where n labels all the eigenstates with existence of z direction trap, $\rho = 1/(e^{\beta(H_{q_x,q_y}-\mu)}+1)$ is the single particle density matrix, and H_{q_x,q_y} is the Hamiltonian in z position space. Here the sum over n is equivalent to sum over k_z and band indices without trap. As a result the k_z integrated spin polarization at (q_x, q_y) point still vanishes with the z direction trap included. Therefore, in the tight binding regime, the position of the band inversion lines (white curves) with consideration of the z direction trap keeps exactly unchanged for the k_z integrated spin textures.

In our experiment, the real system is beyond two band tight binding model due to the Raman coupling between s and p band. So we calculate the optical lattice with trapping potential using plane wave expansion method. Now the k_z is no more good quantum number since the trapping potential scatters the k_z momentum. Therefore, in our system the nth eigenstate at the Bloch momentum (q_x, q_y) takes the form

$$\begin{aligned} |\psi_{q_x,q_y,n}\rangle =& \phi_{q_x,q_y,n}(M,N,k_z,\uparrow)|q_x+2Mk_0, q_y+2Nk_0, k_z+k_2/2,\uparrow\rangle \\ &+ \phi_{q_x,q_y,n}(M,N,k_z,\downarrow)|q_x+k_0+2Mk_0, q_y-k_1+2Nk_0, k_z-k_2/2,\downarrow\rangle. \end{aligned} \tag{S38}$$

Here M, N are integers, and $\phi_{q_x,q_y,n}(M,N,k_z,\sigma)$ denotes the coefficient of the plane waves. In the numerical simulation, to determine and diagonalize the Hamiltonian matrix, we choose the discretized momentums and positions as

$$\begin{aligned} k_{z_i\uparrow} &= \frac{2\pi K_m(2i-L_z-1)}{(L_z-1)a} + \frac{k_2}{2}, \quad i=1,2,3,\cdots,L_z, \\ k_{z_i\downarrow} &= \frac{2\pi K_m(2i-L_z-1)}{(L_z-1)a} - \frac{k_2}{2}, \quad i=1,2,3,\cdots,L_z, \\ z_i &= \frac{(2i-L_z-1)(L_z-1)a}{2L_zK_m}, \quad i=1,2,3,\cdots,L_z. \end{aligned} \tag{S39}$$

Here the parameter K_m controls the momentum cut-off and L_z controls the number of momentums (position space coordinates). The low energy results converge for sufficiently large K_m and L_z. The real matrix elements of the trapping potential are calculated by the integral

$$\begin{aligned} V_{k_z,k_z'} =& \langle q_x+2Mk_0, q_y+2Nk_0, k_z+\sigma k_2/2,\sigma|V_{trap}|q_x'+2M'k_0, q_y+2N'k_0, k_z'+\sigma' k_2/2,\sigma'\rangle \\ =& \delta_{q_x,q_x'}\delta_{q_y,q_y'}\delta_{M,M'}\delta_{N,N'}\delta_{\sigma,\sigma'}V_{k_z,k_z'}. \end{aligned} \tag{S40}$$

To investigate the effect of trap on the system, we define the k_z projected particle number

$$n(q_x,q_y,k_z) = \mathrm{Tr}_n(\hat{P}_{k_z}\rho), \tag{S41}$$

and k_z projected spin polarization

$$S_z(q_x,q_y,k_z) = \frac{\mathrm{Tr}_n(\hat{P}_{k_z}\hat{\sigma}_z\rho)}{\mathrm{Tr}_n(\hat{P}_{k_z}\rho)}. \tag{S42}$$

where $\hat{P}_{k_z}$ is the k_z projection operator defined by

$$\hat{P}_{k_z} = \sum_{q_x,q_y,M,N,\sigma} |q_x+2Mk_0, q_y+2Nk_0, k_z+\sigma k_2/2,\sigma\rangle\langle q_x+2Mk_0, q_y+2Nk_0, k_z+\sigma k_2/2,\sigma|. \tag{S43}$$

As can be seen in Fig. S3 (b,c,d) for the points on the white curves, the magnetic group symmetry are approximately satisfied, i.e.,

$$\begin{aligned} n(q_x, q_y, k_z) &\approx n(q_x, q_y, -k_z), \\ S_z(q_x, q_y, k_z) &\approx -S_z(q_x, q_y, -k_z). \end{aligned} \tag{S44}$$

Thus one can immediately obtain that

$$\mathrm{Tr}_n(\hat{P}_{k_z}\hat{\sigma}_z\rho) \approx -\mathrm{Tr}_n(\hat{P}_{-k_z}\hat{\sigma}_z\rho). \tag{S45}$$

Therefore, the total spin polarization

$$\begin{aligned} S_z(q_x, q_y) =& \frac{\mathrm{Tr}_n(\hat{\sigma}_z\rho)}{\mathrm{Tr}_n(\rho)} \\ =& \sum_{k_z} \frac{\mathrm{Tr}_n(\hat{P}_{k_z}\hat{\sigma}_z\rho)}{\mathrm{Tr}_n(\rho)} \end{aligned} \tag{S46}$$

approximately vanishes due to the anti-symmetric distribution of $S_z(q_x, q_y, k_z)$. We further show the numerical results for the k_z integrated spin textures in Fig. S4(c). One can find that the k_z integrated spin textures with z direction trap are equivalent to the k_z integrated spin textures without trap in Fig. S4(b), which are equivalent to the spin textures of $k_z = 0$ layer without trap in Fig. S4(a). We also plot the example wave functions with existence of z direction trap in Fig. S6 to show the effect of the trap on eigenstates. With the trapping potential included, the k_z distribution of eigenstates are broadened from δ function to finite width with the magnetic group symmetry $\mathcal{M}_z = \sigma_x K$ kept.

Similar to the z direction trap, without calculation, we expect that when x, y direction trapping potential are also included, the (q_x, q_y) projected spin textures measured by experiment are almost the same with that of the theoretically described Bloch Hamiltonian.

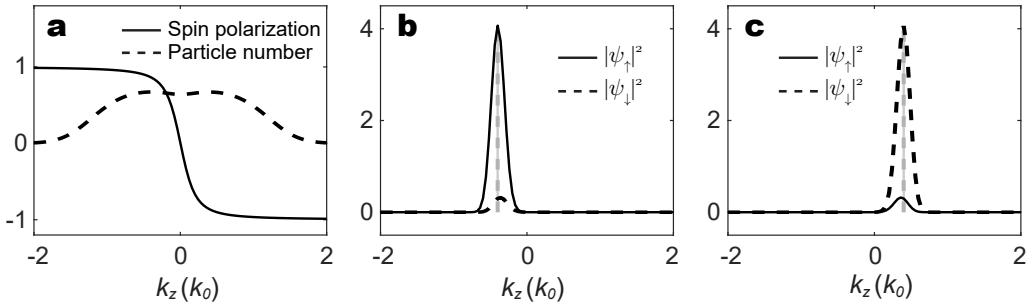

Figure S6: Effect of z direction trapping potential on wave functions. The results are calculated with plane wave expansion. The parameters are set as $(V_{x\uparrow}, V_{x\downarrow}, V_{y\uparrow}, V_{y\downarrow}, M_R, m_z, m\omega_z^2 a^2/2) = (2.3, 1.6, 2.3, 3.0, 0.68, 0, 0.002)E_r$. $(q_x, q_y) = (-0.475, -0.275)k_0$. (a) k_z projected particle number and spin polarization versus k_z for the lowest band without trapping potential. $T = 0.42E_r$, $\mu = 0.14E_r$. (b)-(c) wave functions of the lowest two eigenstate (nearly degenerate). The vertical grey lines denote the wave function without trap (δ functions).

B. Quench dynamics

As a counterpart to the equilibrium state study, we also explore the quench dynamics [2] in our system, where the inter-band oscillation and time-averaged spin texture in the quench dynamics also reveal the 2D Dirac semimetal phase. In our experiment, the Zeeman energy m_z is quenched from a deep trivial regime with $m_z^i = -4.6E_r$ to a

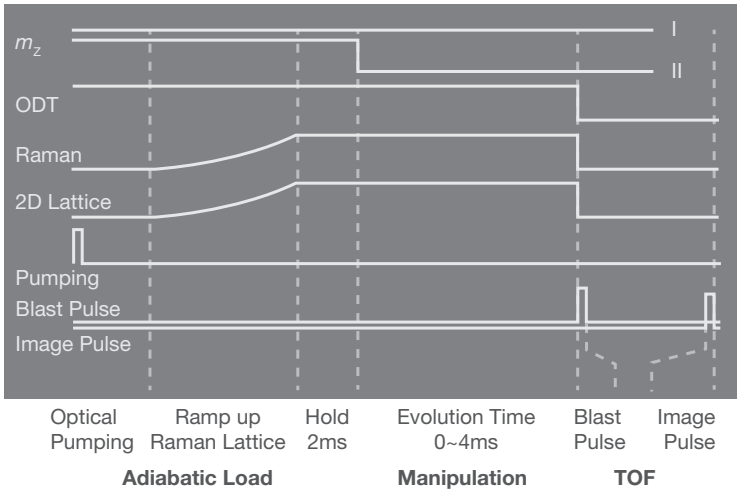

Figure S7: Experimental sequence is described for spin texture imaging in equilibrium (I) and after the quantum quench (II).

non-trivial Dirac semimetal phase with $m_z^f = 0.20(7)E_r$. Without considering the trapping potential, for a single $k_z = 0$ layer, the 1D tight binding Hamiltonians $H_{q_y}(q_x)$ have the following form

$$H_{q_y}(q_x) = \overrightarrow{\mathbf{h}} \cdot \overrightarrow{\boldsymbol{\sigma}} = h_z(q_x)\sigma_z + h_y(q_x)\sigma_y = [m_z'(q_y) - 2t_{x+}\cos q_x a]\sigma_z + 2t_{so}\sin q_x a\sigma_y. \tag{S47}$$

Here the σ_0 term has been discarded as it only contributes a global phase. The initial state is prepared in the deep trivial regime where all the spins are fully polarized up. Without considering an inter-band decay, the time-dependent single particle wave function has the form [5]

$$|\psi(q_x,t)\rangle = e^{-iH_{q_y}(q_x)t}|\psi(q_x,0)\rangle = [-ih_z\sin(E_q t) - E_q\cos(E_q t), h_y\sin(E_q t)]^T, \tag{S48}$$

where $E_q = \sqrt{h_y^2 + h_z^2}$ is the eigenenergy of the Hamiltonian. The spin polarization is then [5]

$$S_z(q_x,t) = \frac{h_z^2 + \cos(2E_q t)h_y^2}{h_y^2 + h_z^2}. \tag{S49}$$

It is clear that only at the BIS point where $h_z(q_x) = 0$ the time averaged spin polarization will vanish. Furthermore, with the inter-band decay included via the Lindblad form master equation in Eq. (S12), the BIS points still have zero time averaged spin polarization as shown in Fig. S1(c). The main effect of the inter-band decay is that the final steady state eventually approaches the ground state of the two band model while the inter-band oscillation can persist over several periods. Thus one can determine the topology of the 1D model by the time-averaged spin texture and verify the 2D Dirac semimetal phase. As a simulation to experiment, the single k_z layer should be replaced by a k_z domain around $k_z = 0$ for the final several periods. As a result, the time-averaged spin texture become blurred as shown in Fig. 4(b) in the main text.

III. Experimental procedure

A. Experimental procedure

A brief experimental sequence is described in Fig. S7. After evaporative cooling in a crossed dipole trap, atoms are adiabatically loaded into an optical Raman lattice by exponentially ramping up Raman lattice beams within 10 ms, followed by 2 ms hold. During the ramp-up process, the Zeeman energy m_z is kept constant for spin-texture

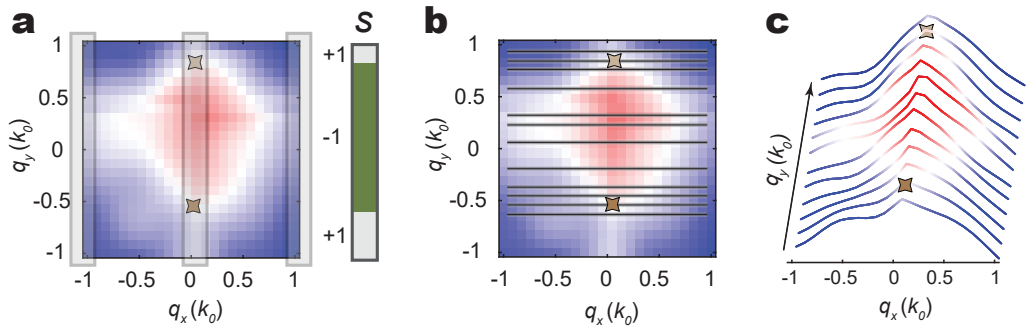

Figure S8: Determination of the Dirac points. (a) In the first method, the quasi-momentum position of the Dirac point is determined by a sign product $\mathcal{S} = sign(P(q_x = 0, q_y) \cdot P(q_x = 1k_0, q_y))$. (b) In the second method, the Dirac point is measured as the spin-flip position. (c) Slice view of the spin texture of (b). The spin polarization varies along the q_y direction.

imaging in equilibrium, whereas suddenly changed for monitoring the quench dynamics. For the quench dynamics, a spin-polarized gas is prepared by optical pumping before the lattice ramp-up. Following a blast pulse, a spin-sensitive absorption image is taken after time-of-flight expansion.

B. Determination of the position of the Dirac points

We apply two methods to determine the momentum positions of the Dirac points from the result of spin texture measurement (see Fig. S8). First method is based on the topological phase transition points along the q_y direction in the spin textures. We first calculate the spin polarization along the $q_x = 0$ and $q_x = k_0$ direction at different m_z, $P(q_x = 0, q_y)$ and $P(q_x = q_0, q_y)$ respectively. Next, we calculate a product of sign, $\mathcal{S} = sign(P(q_x = 0, q_y) \cdot P(q_x = 1k_0, q_y))$ (example shown in Supplementary Information). To be noted, here the value of $\mathcal{S}$ distinguishes different phases. Finally the positions of the Dirac points are determined by the sign-flip position q_{D1} along the q_y direction for each m_z. Second method is based on the boundary between spin-↑ and ↓ domain in the spin textures. Spin-flip positions q_{D2} along $q_x = 0$ and $q_x = 1k_0$, determine the locations of the Dirac points for $m_z > 0$ and $m_z < 0$ respectively. The Dirac point position extracted from these two methods are consistent within the experimental uncertainty.

[1] T. F. J. Poon, X.-J. Liu, From semimetal to chiral Fulde- Ferrell superfluids. Phys. Rev. B **97**, 020501 (R) (2018).
[2] Lin Zhang, Long Zhang, Sen Niu, Xiong-Jun Liu, Science Bull. **63**, 1385 (2018).
[3] A. Altland and Martin R. Zirnbauer, Nonstandard symmetry classes in mesoscopic normal-superconducting hybrid structures. Phys. Rev. B **55**, 1142 (1997).
[4] Chuanzhou Zhu et al 2016 J. Phys. B: At. Mol. Opt. Phys. **49** 145301.
[5] Wei Sun, Chang-Rui Yi, Bao-Zong Wang, Wei-Wei Zhang, Barry C. Sanders, Xiao-Tian Xu, Zong-Yao Wang, Jörg Schmiedmayer, Youjin Deng, Xiong-Jun Liu, Shuai Chen, Jian-Wei Pan, Phys. Rev. Lett. **121**, 250403 (2018).